

1 On the diurnal cycle of deep convection, high clouds
2 and upper troposphere water vapor in the
3 Multi-scale Modeling Framework

Yunyan Zhang,¹ Stephen A. Klein,¹ Chuntao Liu,² Baijun Tian,³ Roger T. Marchand,⁴

John M. Haynes,⁵ Renata B. McCoy,¹ Yuying Zhang,¹ Thomas P. Ackerman⁴

Yunyan Zhang, Atmospheric, Earth & Energy Division, Lawrence Livermore National Laboratory, L-103, P.O. Box 808, Livermore, CA 94551, USA. (zhang25@llnl.gov)

¹Lawrence Livermore National Laboratory, Livermore, California, USA.

²Department of Meteorology, University of Utah, Salt Lake City, Utah, USA.

³Joint Institute for Regional Earth System Science and Engineering,
University of California, Los Angeles, CA, USA.

⁴Joint Institute for the Study of the Atmosphere and Ocean, University of Washington,
Seattle, Washington, USA.

⁵Department of Atmospheric Science, Colorado State University, Fort Collins, Colorado, USA.

1 **Abstract.** The Multi-scale Modeling Framework (MMF, also called “super-
2 parameterization”) embeds a cloud resolving model (CRM) at each grid col-
3 umn of a general circulation model to replace traditional parameterizations
4 of moist convection and large-scale condensation. This study evaluates the
5 diurnal cycle of deep convection, high clouds and upper troposphere water
6 vapor by applying an infrared (IR) brightness temperature (T_b) and a pre-
7 cipitation radar (PR) simulator to the CRM column data. Simulator results
8 are then compared with IR radiances from geo-stationary satellites and PR
9 reflectivities from the Tropical Rainfall Measuring Mission (TRMM). While
10 previous study has shown that the actual surface precipitation rate in the
11 MMF has a reasonable diurnal phase when compared with observations, the
12 IR simulator results indicate an inconsistency in the diurnal anomalies of pre-
13 cipitation and high clouds between the model and the geo-stationary satel-
14 lite data. Primarily due to its excessive high clouds, the MMF overestimates
15 the simulated precipitation index (PI) and fails to represent the diurnal cy-
16 cle phase relationships among PI, high clouds and upper troposphere rela-
17 tive humidity. The PR simulator results show that over tropical ocean, the
18 occurrence fraction of reflectivity in excess of 20 dBZ is almost one magni-
19 tude larger than the TRMM data especially at altitudes above 6 km. Both
20 results suggest that the MMF oceanic convection is overactive and possible
21 reasons for this bias are discussed. However, from the joint distribution of
22 simulated IR T_b and PR reflectivity, the most intense deep convection is found

¹ more often over tropical land than ocean, which agrees with previous obser-
² vational studies.

1. Introduction

1 Climate modeling is a challenging and demanding task. Much of the uncertainty in
2 predicting climate is attributed to cloud and cloud-related processes [Arakawa, 1975;
3 Houghton et al., 2001], which usually can not be resolved but are highly parameter-
4 ized in general circulation models (GCMs). Improved representations of these processes
5 are always at the heart of the model development and the effort has been ongoing for
6 decades [Arakawa, 1969; Randall et al., 2003]. Recently a key breakthrough, the Multi-
7 scale Modeling Framework (MMF, or “super-parameterization”), was proposed to solve
8 the deadlocked situation on convection and cloud parameterizations in GCMs [Grabowski
9 and Smolarkiewicz, 1999; Grabowski, 2001; Khairoutdinov and Randall, 2001; Randall
10 et al., 2003; Khairoutdinov et al., 2005; Tao et al., 2007]. In the MMF, a cloud resolving
11 model (CRM) is implemented at each GCM grid column, replacing the traditional physics
12 parameterizations for moist convection and large-scale condensation. Such an approach
13 is a compromise in the pathway of climate modeling between “parameterize everything”
14 and “resolve everything” [Arakawa, 2004; Khairoutdinov et al., 2005].

15 Parallel to model development, a mandatory task is to make hand-in-hand evaluations
16 to recognize the latest advances and to reveal remaining deficiencies. To correctly produce
17 the diurnal cycle is one of the important measures in model evaluations [Randall et al.,
18 1991; Yang and Slingo, 2001; Tian et al., 2004].

19 The diurnal cycles of deep convection and precipitation have been investigated inten-
20 sively in observational studies with data from different platforms: rain gauge [Gray and
21 Jacobson, 1977; Dai et al., 1999] and weather reports [Kraus, 1963; Dai, 2001], ground-

1 based radar [*Short et al.*, 1997], satellite infrared sensors [*Short and Wallace*, 1980; *Soden*
2 *et al.*, 2000; *Yang and Slingo*, 2001; *Tian et al.*, 2004], satellite microwave sensors [*Chang*
3 *et al.*, 1995], and the precipitation radar on board the Tropical Rainfall Measuring Mission
4 (TRMM) satellite [*Nesbitt and Zipser*, 2003; *Liu and Zipser*, 2008]. Most of these studies
5 show that the deep convection and precipitation maxima occur most frequently in the
6 early morning over open oceans and in the late afternoon/early evening over continents.
7 Using geo-stationary satellite infrared radiances, *Tian et al.* [2004] demonstrated that the
8 diurnal maximum of clear-sky upper troposphere relative humidity (UTH) lags the high
9 cloud amount maximum, and that the latter lags the deep convection and precipitation
10 maximum. Moreover using TRMM data, *Zipser et al.* [2006] and *Liu et al.* [2007] showed
11 that extreme intense convection is found more often over land than ocean.

12 It is generally accepted that the diurnal late-afternoon/early-evening precipitation max-
13 imum over land is a thermodynamic response to the surface solar heating. While there
14 is no consensus on the open ocean precipitation maximum in the early morning, three
15 mechanisms have been proposed. The first involves the direct effects of radiation on cloud
16 radiative heating: during the night (daytime), longwave radiative cooling (solar heating)
17 enhances (inhibits) convection [*Kraus*, 1963; *Randall et al.*, 1991]. The second argues that
18 the horizontal differential radiative cooling induces a diurnal variation in the divergence
19 field, which results in greater low-level moisture convergence and precipitation in the early
20 morning [*Gray and Jacobson*, 1977]. The third attributes the diurnal cycle to both the
21 lifetime of large scale convective systems and a more complex interaction between clouds,
22 radiation and near-surface thermodynamics [*Chen and Houze*, 1997; *Sui et al.*, 1997].

1 Several studies [*Khairoutdinov et al.*, 2005; *Wyant et al.*, 2006; *Ovtchinnikov et al.*, 2006;
2 *DeMott et al.*, 2007; *McFarlane et al.*, 2007; *Marchand et al.*, 2007] have compared the
3 MMF with observations and traditional GCMs, such as the NCAR Community Atmo-
4 sphere Model (CAM). Specifically *Khairoutdinov et al.* [2005] showed that relative to the
5 CAM, the MMF improves the diurnal phase of non-drizzle precipitation frequency. In
6 this paper, we investigate the diurnal variation of precipitation, deep convective and anvil
7 clouds, and upper troposphere water vapor as well as the occurrence frequency of deep
8 convection and updraft intensity.

9 In using a “model-to-satellite” approach [*Morcrette*, 1991; *Klein and Jakob*, 1999], we
10 apply an infrared (IR) brightness temperature (T_b) [*Soden et al.*, 2000; *Tian et al.*, 2004]
11 and a precipitation radar (PR) simulator (QuickBeam, *Haynes et al.* [2007]) to the MMF
12 CRM column data to measure cloud condensate and precipitation, respectively. Simulator
13 results are then compared with IR radiances from geo-stationary satellites [*Tian et al.*,
14 2004] and PR reflectivities from TRMM [*Zipser et al.*, 2006; *Liu et al.*, 2007]. In this
15 study, we try to answer the following questions:

16 1. Is the MMF able to capture the diurnal cycle of deep convection, high clouds and
17 the clear-sky UTH?

18 2. Is the MMF able to represent correctly the frequency and intensity of deep convec-
19 tion, particularly the land-sea contrast in the nature of deep convection?

20 In section 2, we detail the MMF simulations, observational datasets, and the simulators.
21 The IR and PR simulator results are presented in section 3 and 4 respectively. In section 5,
22 we examine the properties of deep convection and its land-sea contrast by considering the
23 joint distribution of IR T_b and PR reflectivity. Section 6 discusses sensitivity tests and

1 factors that may be accountable for the model biases, while a summary is presented in
2 section 7.

2. The Model, observations and simulators

2.1. The MMF simulations

3 The MMF consists of two components: the parent GCM and the embedded CRM at
4 each GCM grid column. The MMF simulation were conducted by Thomas Ackerman
5 and Roger Marchand at the Pacific Northwest National Laboratory (now both at the
6 University of Washington, Joint Center for the Study of Atmosphere and Ocean) using
7 the model created by Khairoutdinov and Randall [*Khairoutdinov et al.*, 2005], except
8 that the GCM — the NCAR CAM 3.0. [*Collins et al.*, 2006] — includes the finite-volume
9 dynamical core instead of the semi-Lagrangian dynamical core. CAM 3.0 is run with 26
10 vertical levels and a horizontal resolution of 2° latitude and 2.5° longitude.

11 The CRM is the System for Atmospheric Modeling (SAM) [*Khairoutdinov and Randall*,
12 2003]. SAM is configured as a 2-dimensional CRM with 64 grid columns at each GCM
13 grid, horizontally aligned along the east-west direction with 4 km spacing and cyclic lateral
14 boundary conditions. It is run with 24 vertical levels, which are collocated with the lowest
15 24 levels in the parent GCM. Because the CRM resolves a distribution of clouds, radiation
16 calculations are performed on each CRM grid column every 15 minutes.

17 The simulation is constrained by the observed distributions of sea surface temperature
18 and sea ice. The MMF simulation is initialized from a CAM restart and spans June 1998
19 to June 2002. In this simulation, 3 hourly "snap-shots" of the MMF CRM condensate
20 and water vapor fields along with more typical temporal and spatial averages of these
21 fields were output at each of the GCM grid boxes. Although the results presented below

1 are only for July 1999, investigation has been performed for several other months (such
2 as January and July 2000) and thus we will not discuss these results unless they differ.

2.2. Observation

3 Two observational datasets are used: geo-stationary satellite infrared radiances [*Tian*
4 *et al.*, 2004] and TRMM precipitation radar reflectivities [*Liu et al.*, 2007; *Liu and Zipser*,
5 2008].

6 IR radiances are denoted by equivalent black body brightness temperatures (T_b) in
7 water vapor ($6.7 \mu\text{m}$, $T_{6.7}$) and window ($11 \mu\text{m}$, T_{11}) channels. The 3-hourly T_b data
8 from July 1999 are used at a pixel resolution of 0.1° longitude-latitude between 30°N and
9 30°S . Based on T_{11} and $T_{6.7}$, we retrieve a precipitation index (PI), high cloud amount
10 (CLD) and clear-sky upper tropospheric relative humidity (UTH) at each pixel. The
11 retrieval algorithm is summarized in Table 1 and interested readers may refer to *Tian*
12 *et al.* [2004] and *Soden and Bretherton* [1993, 1996] for details.

13 The precipitation radar on the TRMM satellite [*Kummerow et al.*, 1998] measures re-
14 flectivity with a horizontal resolution of 4.3 km by 4.3 km at nadir and a vertical resolution
15 of 250 meters from the surface to 20 km. At the frequency of 13.8 GHz, the measured re-
16 flectivity is primarily sensitive to precipitation hydrometeors. In this study, the University
17 of Utah TRMM database [*Nesbitt et al.*, 2000; *Liu et al.*, 2007] provides the occurrence cli-
18 matology of 20 dBZ or greater reflectivity at different altitudes. A reflectivity of 20 dBZ or
19 greater signifies precipitation has been detected [*Liu et al.*, 2007]. The 20 dBZ or greater
20 occurrence climatology is obtained by accumulating 9 years (1998-2006) of TRMM PR
21 pixels with reflectivity ≥ 20 dBZ from 2 km to 15 km at 1 km intervals separately for

1 land and ocean between 20°S and 20°N in the month of July. Data from altitudes below
2 2 km are ignored because of ground clutter.

2.3. The IR T_b and PR simulators

3 The IR T_b simulator is a generalized forward radiative transfer model for HIRS-14 [*Soden*
4 *et al.*, 2000; *Tian et al.*, 2004], which calculates clear-sky and all-sky T_{11} and $T_{6.7}$ from
5 the MMF CRM vertical profiles of temperature, water vapor and cloud condensates. To
6 obtain the cloud emissivity, the ice absorption coefficient is calculated according to *Ebert*
7 *and Curry* [1992] assuming that the ice particle effective radius is an increasing function
8 of temperature and $140 \text{ m}^2/\text{kg}$ is used for the liquid absorption coefficient. We treat
9 every 4 km MMF CRM grid column as if it were a satellite pixel, and apply the retrieval
10 algorithm in Table 1 to each CRM grid column in each GCM grid box.

11 Some studies have remarked that the IR T_b threshold technique in the retrieval algo-
12 rithm does not provide any information from inside clouds as it is only sensitive to cloud
13 top temperatures, which might be similar for deep convective and thick cirrus clouds [*Liu*
14 *et al.*, 1995; *Hall and Haar*, 1999; *Hong et al.*, 2006]. Model evaluations may also suffer
15 from such T_b similarity particularly if there is an over abundance of high clouds [*Slingo*,
16 2004]. Because the PR simulator can overcome this potential deficiency, it is a useful
17 complement to the IR simulator.

18 The PR simulator is QuickBeam [*Haynes et al.*, 2007] (website for codes download —
19 <http://cloudsat.atmos.colostate.edu/radarsim>) version 1.03d with modifications by Roger
20 Marchand to increase computational speed [*Marchand et al.*, 2007]. The inputs are the
21 MMF CRM vertical profiles of temperature, relative humidity and its five hydrometeor
22 species which are cloud ice, cloud water, rain, snow and graupel. The outputs are the

1 vertical profiles of attenuation-corrected volume reflectivity (dBZ) at the frequency of the
2 TRMM radar. QuickBeam allows users to specify different hydrometeor classes based on
3 five types of size distributions: modified gamma, exponential, power law, monodisperse,
4 and lognormal. The assumptions we use are, for cloud water, a lognormal distribution,
5 for cloud ice, a modified gamma distribution [Mitchell *et al.*, 1996], and for rain, snow and
6 graupel, an exponential distribution according to *Marshall and Palmer* [1948] in which
7 fixed intercept parameters are used [Khairoutdinov and Randall, 2003]. The assump-
8 tions on precipitation are the same as those used in the microphysics of the embedded
9 CRM [Khairoutdinov and Randall, 2003].

10 Figure 1 illustrates the application of both simulators to a snapshot of one of the CRMs
11 embedded in the MMF. In the top panel, dots indicate the level where the temperature
12 equals that of the simulated T_b . One can clearly see a close association between this level
13 and the highest level of significant cloud ice or water. In the lower panel, the blue contour
14 lines show the the reflectivity from the PR simulator, which has a good association with
15 significant amounts of rain, snow and graupel.

3. The MMF vs. Geo-stationary Satellite Data

16 To compare the IR T_b simulator results with geo-stationary satellite data, the PI, CLD
17 and UTH which are calculated at the MMF CRM grid columns are averaged to the GCM
18 grid box in the resolution of 2.5° longitude and 2.0° latitude between 30°S and 30°N . As
19 geo-satellite pixels are likewise averaged, an “apple-to-apple” comparison is possible, in
20 which the IR simulator measures the MMF simulated atmosphere as the real satellites
21 observe the earth. For comparison we also examine MMF’s actual precipitation rate, high
22 cloud amount, and upper tropospheric relative humidity which we calculate from MMF

1 output directly without the use of a simulator. We will refer to these three MMF “actual”
2 quantities with no abbreviations to avoid confusion.

3 Figure 2 shows daily means and diurnal cycles of PI from geo-satellite data (top), PI
4 from IR T_b simulator (middle) and the MMF actual surface precipitation rate (bottom).
5 The diurnal cycle is constructed from 3-hourly data and is decomposed using a Fourier
6 transform [*Tian et al.*, 2004]. Based on the first harmonic, the diurnal amplitude is the
7 half of the difference between maximum and minimum and the diurnal phase arrow points
8 to the local standard time (LST) of the maximum.

9 As PI has been viewed as an indication of precipitation from deep convection in numer-
10 ous studies [*Richards and Arkin*, 1981; *Hendon and Woodberry*, 1993; *Soden et al.*, 2000;
11 *Yang and Slingo*, 2001; *Tian et al.*, 2004], we expect a good relationship between PI and
12 the actual surface precipitation rate. However this is not the case for the MMF, where the
13 tropical and daily mean PI of 13.4 mm/day is in excess of the satellite PI of 2.9 mm/day or
14 the MMF actual precipitation rate of 3.3 mm/day. This difference is especially prominent
15 in the region from east Africa to the west Pacific, where an overestimation of the diurnal
16 amplitude is also found. Moreover, the simulator PI is inconsistent with the satellite PI in
17 the diurnal phase over land regions, such as Africa. In contrast, the MMF actual precip-
18 itation rate displays magnitudes and geographical distributions in the daily means that
19 are comparable to those in the satellite PI, however, the diurnal amplitudes are relatively
20 weak. The satellite PI shows a land-sea contrast with larger diurnal amplitudes over land
21 than over ocean. This is not evident in the MMF actual surface precipitation rate and
22 the diurnal amplitude of the simulator PI is larger over ocean than over land.

1 Figure 3 shows the diurnal anomaly composites for tropical land (right) and ocean (left)
2 of geo-satellite data (top), simulator results (middle) and the MMF actual quantities
3 (bottom). Table 2 shows details of the amplitudes (in bold), daily means (in plain) and
4 normalized amplitudes (in brackets) by dividing the former by the latter.

5 In Figure 3, geo-satellite data display a diurnal phase relationship: over ocean (land),
6 PI peaks at 0600 (1800) LST, follows the CLD maximum at 1500 (2100) LST and the
7 UTH maximum around midnight (0300 LST). The phase lag between PI, CLD, and UTH
8 is about 6-9 hours over ocean and 3-6 hours over land. This illustrates a clear picture that
9 deep convection (inferred from PI) leads to high anvil cloud generation and the anvil cloud
10 dissipation results in moisturizing the upper troposphere [*Tian et al.*, 2004]. Furthermore
11 in Table 2, the geo-satellite data exhibit greater values over land than over ocean with
12 normalized diurnal amplitudes over land triple the corresponding value over ocean for
13 both PI and CLD and double the ocean value for UTH.

14 There are three major inconsistencies between simulator results and the geo-satellite
15 data. First the simulator PI over land peaks at 0600 LST and is out of phase with the
16 satellite data. Second the simulator CLD over ocean has a diurnal maximum at 0600 LST
17 and is out of phase with the satellite observation. Thirdly the diurnal amplitude of the
18 simulator PI over ocean is largely overestimated and is even larger than the one of the
19 simulator PI over land, which is contradictory to the satellite data.

20 Because geo-satellite infrared PI might be biased in representing the actual surface
21 precipitation [*Liu et al.*, 2007], diurnal composites of TRMM PR observed precipitation
22 rate over land and ocean are also shown in Figure 3 and Table 2 to facilitate the “apple-
23 to-apple” comparison with the MMF actual surface precipitation rate. The diurnal phase

1 of the MMF actual precipitation rate agrees well with both geo-satellite data and TRMM
2 data, consistent with *Khairoutdinov et al.* [2005], however the diurnal amplitude is weak
3 especially over land and the daily mean is overestimated especially over ocean. Although
4 the diurnal amplitude of MMF high cloud (from either the simulator or the actual value)
5 is larger over land than over ocean as observed, the diurnal phase is at 0600 LST which
6 contrary to the satellite data over both land and ocean and the daily means almost double
7 the satellite data. In contrast, while the amplitudes are not as large as the satellite
8 data, both the simulator UTH and the MMF actual upper troposphere humidity have a
9 reasonable diurnal phase variation.

10 The simulator PI shows overestimation in the tropical daily means and diurnal ampli-
11 tudes and a diurnal phase error over land, however such behaviors are not found in the
12 MMF actual surface precipitation rate. On the other hand, the MMF actual high cloud
13 amount is double the value in the satellite data but quite consistent with the simulator
14 CLD. Together, these results suggest that MMF has an excessive amount of radiatively
15 significant high cloud. In order to investigate this bias in a more simple manner, we
16 examine the simulator T_{11} and $T_{6.7}$, from which the PI, CLD and UTH are retrieved.

17 Figure 4 shows the probability density function (left) and cumulative probability (right)
18 of T_{11} over tropical land regions. Although not shown, similar behavior of T_{11} and $T_{6.7}$
19 is also found over tropical oceans and in the comparison of less aggregated data, *e.g.*
20 between the CRM grid and the satellite pixel data.

21 Clearly, below 260 K, a cold bias is found in the simulator T_{11} (solid) as compared
22 to satellite data (dashed). If deep convective clouds (DCC, or hot towers) are defined
23 by $T_{11} < 230$ K, the condition which turns on the PI retrieval, then DCC is about 9%

1 from the simulator and only 3% from the satellite data. Since PI is proportional to the
2 difference between 230 K and T_{11} , the colder T_{11} leads to larger PI, thus explaining the
3 bias of the daily mean PI. As for the CLD retrieval, about 21% of the simulator T_{11} are
4 below 260 K compared to 14% in the satellite data. Notice that if the deep convection
5 anvil cloud (CAC) is defined by T_{11} between 230 K and 260 K, instead of T_{11} less than
6 260 K, then it will be 12% from the simulator comparable to 11% from satellite data.

7 If the cold bias in T_{11} explains the overestimation of the daily mean simulator PI and
8 CLD, then how is the diurnal phase error related? Figure 5 and 6 show the histograms
9 of the diurnal probability anomalies of T_{11} and UTH. T_{11} (UTH) data are distributed
10 among 5 k (5%) bins at each 3-hour period. Probabilities are calculated in each bin at
11 each 3-hourly period by dividing the number of data in that bin by the total number of
12 data among all the bins at that time period. Finally diurnal probability anomalies in
13 each bin at each 3-hourly period are acquired by removing the daily mean of that bin to
14 emphasize the diurnal variation. Thus positive (negative) contour suggests at which local
15 times, certain temperature values prefer (dislike) to occur.

16 In Figure 5, the satellite data (reproduced from *Tian et al.* [2004]) show that over land,
17 the DCC ($T_{11} < 230$ K) and CAC (230 K $< T_{11} < 260$ K) maximum tend to occur
18 concurrently in the evening, whereas over ocean, the DCC peaks in the morning while the
19 CAC peaks in the late afternoon. Furthermore satellite T_{11} over land has a larger diurnal
20 variation than over ocean. The most prominent difference shown in simulator results is
21 the diurnal evolution of T_{11} colder and warmer than 220 K. When warmer than 220 K,
22 the simulator T_{11} changes in the same manner as the observation, however with a larger
23 variation over ocean than over land. When colder than 220 K, the simulator T_{11} peaks in

1 the morning and minimizes in the afternoon over both land and ocean. The behavior of
2 T_{11} beneath and above 220 K are out of phase with each other, but with a much larger
3 diurnal variation when T_{11} is colder than 220 K. This explains the diurnal phase error in
4 the simulator PI ($T_{11} < 230$ K) and CLD ($T_{11} < 260$ K) in Figure 3.

5 Given the cold bias in T_{11} as well as the fact that over land the simulator PI is out of
6 phase with MMF actual surface precipitation, we must ask if we are detecting true deep
7 convective hot tower clouds in MMF by selecting CRM columns with $T_{11} < 230$ K. To
8 answer this we examined snapshots like those in Figure 1. The extreme cold T_{11} often
9 coincides with an overcast cloud layer between 400 hPa and 150 hPa, or even higher, and
10 usually persists for several days before dissipation. We also find such high cloud layer
11 sometimes with deep convective cloud tower attached to it and sometimes not. Since the
12 MMF output data is 3-hourly, it is really hardly to say whether these high clouds are
13 anvil clouds associated with deep convection or not. However it is clear that a significant
14 portion of high clouds with IR $T_{11} < 230$ K are not true deep convection hot tower clouds,
15 but these thick long-lasting high clouds. This finding agrees with other MMF evaluation
16 studies. *McFarlane et al.* [2007] pointed out that the MMF largely overestimates the deep
17 convection and thick cirrus cloud occurrence frequency at the tropical western Pacific
18 ARM sites. Using CloudSat cloud radar data, *Marchand et al.* [2007] found that MMF
19 has excessive hydrometeor coverage in several deep convection regions at all altitudes.

20 Figure 4 shows that the discrepancy between observations and simulator results becomes
21 smaller when T_{11} is warmer than 260 K, the criteria which turns on the retrieval of UTH
22 (Table 1). Figure 6 shows the diurnal probability anomaly histogram for UTH in 5% bins.
23 Observations over both ocean and land show that high clear-sky UTH (>70%) maximizes

1 during midnight and minimizes at noon, while low UTH (<70%) tends to behave in the
2 opposite way [*Tian et al.*, 2004]. The simulator UTH agrees with the observation quite
3 well although the MMF underestimates the diurnal amplitude over land and there is a
4 2-3 hour phase lead relative to observations in high UTH.

4. The MMF vs. TRMM data

5 Below we present results for PR reflectivities ≥ 20 dBZ, which is considered as ev-
6 idence of strong convective updrafts that lift more and/or larger ice particles to higher
7 altitudes [*Liu et al.*, 2007].

8 Figure 7 shows the PR 20 dBZ or greater occurrence fraction in July in tropics (20°S-
9 20°N). The occurrence fraction is obtained by dividing the number of TRMM pixels (data
10 at CRM column height levels) with reflectivity ≥ 20 dBZ at a given altitude by the
11 total number of TRMM samples (CRM columns). The occurrence fraction at a certain
12 altitude suggests the potential for deep convective updrafts to reach that altitude. Both
13 the TRMM data and the PR simulator results clearly show that there are less strong
14 updrafts at higher altitudes. For instance, the TRMM data suggests that the potential to
15 observe a deep convective case over land is about 1% at 6 km, 0.1% at 10 km and 0.01%
16 at 14 km.

17 Although there is good agreement over land, over ocean the 20 dBZ or greater occurrence
18 fraction from the PR simulator is almost one order of magnitude larger than the TRMM
19 data, at altitudes above 6 km. This suggests the MMF oceanic deep convection is too
20 frequent resulting in too many strong updrafts that penetrate to high altitudes. TRMM
21 data suggest that deep convection tends to be more active over land than over ocean
22 above 6 km. Such land-sea contrast is not captured in PR simulator results, implying

1 that there is little land-sea distinction in the deep convection occurrence tendency in the
2 MMF. However if we pay attention to extreme intense deep convections represented by
3 PR reflectivities ≥ 40 dBZ, the occurrence fraction is greater over land than ocean in
4 the MMF above 4 km.

5 Figure 8 displays the composite diurnal cycle of the 20 dBZ occurrence fraction in tropics
6 at 6 km, 10 km and 14 km. The TRMM data shows a much more pronounced diurnal
7 variation over land than ocean at all the three levels, however, the PR simulator results
8 behave the opposite way. Over ocean (land), the TRMM data always has a minimum
9 (maximum) at 1800 LST, and maximum (minimum) in the morning. While the simulator
10 results generally indicate similar phase to the maxima and minima, the amplitude of the
11 diurnal variation is far too small over land at all the three levels and too large over ocean
12 at 10 and 14 km. Note that the underestimate in land diurnal amplitude becomes less in
13 winter months, *e.g.* January. Furthermore at 14 km, the occurrence fraction over land
14 has a secondary peak at 0600 LST which is inconsistent with the TRMM data; this might
15 be related to the phase error found in PI and CLD from the IR T_b simulator shown in
16 Figure 3.

5. Results from the joint distribution of MMF simulated IR T_b and PR Reflectivity

17 What can we learn about MMF deep convection by using both simulators simultane-
18 ously? Here, we investigate the statistics of CRM columns with both IR $T_{11} < 230$ K
19 and PR reflectivity ≥ 20 dBZ anywhere in the vertical column, which may be a better
20 indicator of deep convective clouds than either measure individually.

1 The color shading in Figure 9 depicts at each GCM grid box in the MMF, the probability
2 (in percent) to detect a deep convective CRM column using different measures: both
3 simulators (top); the IR T_b simulator only (middle); and the PR simulator only (bottom).
4 More than 50% of the CRM columns are observed to have $T_{11} < 230$ K in regions from
5 the Indian Ocean to the Northwest Pacific, and more than 30% in East cenral Africa and
6 the Arabian Peninsula. However the top panel demonstrates that in these regions, lower
7 than 30% of the CRM columns with $T_{11} < 230$ K have radar reflectivity ≥ 20 dBZ.
8 Although some deep convection clouds may not produce precipitation if they are still in
9 the initial stage of development, this probability can not explain this large difference.
10 Rather this suggests that a large portion of clouds with $T_{11} < 230$ K in the MMF are not
11 deep convective clouds (DCCs), which further confirms our finding in section 3. On the
12 other hand, comparison between the top and bottom panels of Figure 9 reminds us that
13 some convective CRM columns detected by the PR simulator with reflectivity ≥ 20 dBZ
14 may not penetrate deep enough to have the cloud top $T_{11} < 230$ K; this is particularly
15 true over central Africa and Amazon.

16 If we define deep convective hot tower clouds as those CRM columns which jointly have
17 IR $T_{11} < 230$ K and PR reflectivity ≥ 20 dBZ, can we detect land-ocean difference
18 in the intensity of convection in MMF? Figure 10 shows the cumulative probability of
19 in-cloud melting-level updrafts of these CRM columns. Melting level is determined by the
20 vertical profile of temperature at each of the CRM columns. Each data point represents
21 the probability of the updraft above certain limit, e.g., only about 10% of these columns
22 have updrafts greater than 1.5 m/s. Note that we are examining only the 50% of these
23 columns for which the instantaneous vertical velocity is upward at the melting level.

1 Although this may suggest that in MMF the convective updrafts are weak, compared to
2 observations which indicate values above 10 m/s [*Zipser et al.*, 2006; *Liu et al.*, 2007],
3 our use of 3-hourly snapshot data may hinder a definitive assessment. However in the
4 tail of the updraft distribution, we do find more deep convective hot towers with stronger
5 updrafts over land relative to ocean. For example, about 0.3% of the MMF hot towers
6 have updrafts in excess of 8.5 m/s over land whereas only 0.1% of the hot towers over
7 ocean have updrafts in excess of this value.

8 Figure 11 shows the probability for PR reflectivity of 20 dBZ or greater to be found at
9 a given height in each 1 m/s bin of the deep-convective in-cloud melting-level updrafts.
10 The probability is obtained by dividing the number of CRM columns with 20 dBZ or
11 greater at a given height in a given updraft bin by the total number of CRM columns in
12 the same bin. Although there is sampling noise at large values of updraft strength, it is
13 clear that with increasing updraft strength, precipitation particles penetrate to a higher
14 altitude, which is consistent with the assumption that radar reflectivity is proportional to
15 convective intensity. Moreover, at same updraft strength, precipitation particles reach a
16 greater depth over land than over ocean. This suggests that the MMF is able to represent
17 some aspects of the observed land-sea contrast [*Zipser et al.*, 2006; *Liu et al.*, 2007].

18 If we recompute the precipitation index (in Figure 2 and 3) from those CRM columns
19 that have both IR $T_{11} < 230$ K and PR reflectivity ≥ 20 dBZ, we still find a diurnal
20 phase bias over land although the daily mean overestimation (Table 2) is no longer present.
21 This suggests that these early morning clouds are precipitating which helps to explain why
22 the diurnal cycle amplitude of the actual surface precipitation in MMF is so weak.

6. Discussion

6.1. Uncertainties in the model-observation comparison

1 In the computation of infrared T_b , the radiative properties of cloud ice and water are
2 speculated from *Ebert and Curry* [1992] and are identical to those used in the CAM. The
3 most sensitive parameter is the ice mass absorption coefficient, k_i . If we reduce k_i to 1/3
4 of its original value, the cold bias shown in Figure 4 decreases and the simulated $T_{6.7}$ and
5 T_{11} are comparable to the observed values. However, such reduction lowers the value of k_i
6 outside of its uncertainty range (Q. Fu and X. Huang, personal communications). Even
7 with this reduction, the phase bias of PI and CLD shown in Figure 3 remains.

8 Radar simulators are sensitive to the assumed size distribution of the precipitation
9 hydrometeors. We use those of *Marshall and Palmer* [1948], which are identical to those
10 assumed by the embedded CRM in its calculation of bulk microphysical process rates.
11 Although the simulation would be different, we treated the graupel in the radar simulator
12 as if it were snow, effectively reducing the equivalent volume sphere size of the graupel
13 particles. This significantly reduces the 20 dBZ occurrence fraction, particularly between
14 6 km and 10 km in Figure 7. These altitudes are just above the freezing level in the
15 tropics where the temperature dependent partitioning of hydrometeor assumes graupel
16 occurs. However, this change removes only about 15% of the oceanic overestimation by
17 MMF shown in Figure 7 and 8.

6.2. Why biased?

18 Given that the conclusion that MMF has an excessive amount of high clouds and precip-
19 itation hydrometeors particularly over ocean is robust to uncertainties in the comparison
20 of model to observations, the next question is what are the causes of this bias? Below

1 we present some possible causes of this bias, but we do not judge which are responsible
2 as this requires a large number of experiments which is not feasible given MMF's heavy
3 computational expense.

4 The overestimate in high clouds may result from errors in the cloud formation and
5 dissipation. To form clouds, moisture supply is a must, which must come from vertical
6 transports. From the PR simulator, we know that MMF deep convection over ocean is
7 overactive by almost one magnitude in 20 dBZ or greater occurrence fraction, especially
8 at the altitudes above 6 km. One possible interpretation of this result is that with too
9 frequent oceanic deep convection, MMF overestimates the moisture transported from
10 lower to upper troposphere, favoring the high cloud generation.

11 The extensiveness of high clouds could be attributed to the lack of strong penetrating
12 updrafts. Specifically, if there are not enough convective updraft overshoots at the top of
13 deep convective clouds, the compensating subsidence will be weak and unable to limit the
14 expansion of convective anvil clouds. Figure 10 suggests that the convective updrafts in
15 MMF are weak and this is presumably related to the coarse resolution of the MMF CRM
16 in both the horizontal and vertical dimensions. *Khairoutdinov and Randall* [2003] showed
17 that the variance of vertical velocity in SAM increases with finer horizontal resolution. In
18 a CRM radiative-convective equilibrium study, *Pauluis and Garner* [2006] showed that a
19 coarser resolution may lead to flat parcels rising with a slower pace; however, they also
20 showed this might not affect reasonable deep convection cloud ice and vertical velocity
21 distribution.

22 The cyclic lateral boundary condition of the MMF CRM may contribute to the high
23 cloud overestimation as the clouds and moisture reenter the CRM domain rather than

1 advecting away. Additionally, impacts with a 3-dimensional CRM in the MMF instead
2 of the default 2-dimensional CRM have demonstrated significant influence on tropical
3 precipitation and water vapor [*Khairoutdinov et al.*, 2005].

4 The MMF CRM uses a simple bulk microphysics parameterization [*Khairoutdinov and*
5 *Randall*, 2003], in which the partitioning between hydrometeors is solely temperature
6 dependent. The dissipation of high clouds is affected by the terminal velocities of hy-
7 drometeors and the parameterized rates of ice autoconversion and aggregation. Changes
8 in these parameterizations will certainly lead to changes in cloud condensate and precipi-
9 tation and may significantly affect the high cloud bias. Furthermore, observations indicate
10 that the particle size distributions on land and ocean are very different [*Rosenfeld and*
11 *Lensky*, 1998], however there is no distinct treatment in the model. This may affect the
12 PR 20 dBZ statistics since the radar signal is very sensitive to the particle size.

7. Summary

13 In this study we evaluate the diurnal cycle of high cloud, upper tropospheric water vapor
14 and precipitation in the MMF by applying the IR T_b and PR simulators to the CRM grid
15 scale. The precipitation index (PI), high cloud amount (CLD) and upper tropospheric
16 relative humidity (UTH) from the IR T_b simulator are compared to geo-stationary satellite
17 data and the occurrence of the reflectivity greater than 20 dBZ from the PR simulator is
18 compared to the TRMM data. Combining both simulators, the properties of convective
19 updrafts are investigated.

20 From the satellite observations [*Tian et al.*, 2004], a phase-lag relationship in the diurnal
21 cycle is evident with the clear-sky UTH maximum following the CLD maximum and the
22 latter following the PI maximum with 3-6 hours apart over land and 6-9 hours apart

1 over ocean. The amplitudes of the diurnal cycle are observed to be stronger over tropical
2 land than ocean. Our study shows that the phase relationship and land-sea difference
3 in amplitudes are not well simulated in the MMF. The IR simulator PI over land is out
4 of phase with geo-satellite observations. The MMF actual surface precipitation rate is
5 compared with both geo-satellite PI and TRMM PR observed precipitation rate. This
6 shows that the diurnal phase is consistent with observations while the diurnal amplitude
7 is weak especially over land and daily mean value over ocean is overestimated. Both the
8 simulator CLD and the MMF actual high cloud amount over ocean are out of phase with
9 the observed one. Furthermore the daily mean of the simulator PI and CLD and the MMF
10 actual high cloud amount are greatly overestimated. Many of these biases are attributed
11 to the cold bias in the T_b , which results from an excessive amount of high clouds in MMF.
12 Despite this, clear-sky UTH tends to agree well with observations in both daily mean and
13 the diurnal variation.

14 Based on the occurrence of 20 dBZ or greater reflectivity from the PR simulator, we find
15 that over tropical ocean, the MMF deep convection occurs much more frequently than
16 in the TRMM observations. Moreover, MMF exhibits little distinction between tropical
17 land and ocean in the occurrence fraction of reflectivity ≥ 20 dBZ, contrary to TRMM.
18 However, extremely intense convection with reflectivity ≥ 40 dBZ is found more often
19 over land than ocean. In examination of the diurnal cycle, MMF underestimates the
20 occurrence of 20 dBZ reflectivity over land particularly at 1800 LST, the time of local
21 diurnal maximum. Over ocean, MMF overestimates the occurrence of 20 dBZ reflectivity
22 during the whole diurnal cycle at each of the three levels examined (6, 10 and 14 km).

1 From the CRM columns in which PR reflectivity ≥ 20 dBZ and IR $T_{11} < 230$ K
2 co-occur, we examine the properties of deep convective towers. The vertical velocities in
3 these towers appear to be weak. However, the analysis also shows that stronger updrafts
4 penetrate deeper and that extremely intense updrafts are found more often over land than
5 over ocean.

6 In spite of these problems in the simulation of the diurnal cycle, MMF is still superior to
7 conventional GCMs in many aspects. The diurnal maximum of the MMF actual surface
8 precipitation rate occurs at sunset over land whereas GCMs tend to simulate precipitation
9 maximums closer to noon. *Tian et al.* [2004] showed that the GFDL AM2 was not able
10 to capture the behavior of UTH, especially in the histogram analysis such as in Figure 6,
11 which the MMF does well. Moreover the MMF captures some aspects of the land-sea
12 contrast in that intense deep convection is found more often over land than over ocean
13 and usually penetrates deeper. Conventional GCMs may have difficulty in doing this,
14 although one study suggests that it is feasible [*Del Genio et al.*, 2007]. Despite all this,
15 the problems in MMF are great enough to cast doubt on the ability to use MMF as a basis
16 for improvement of the diurnal cycle of cloud and precipitation in conventional GCMs.

17 This study shows that it is efficient and reasonable to use simulators to compare the
18 MMF to global observations. It would be of interest to repeat this study with other
19 MMFs [*Tao et al.*, 2007] or a global cloud resolving model [*Miura et al.*, 2007]. In the near
20 future, we will investigate the impact of ongoing improvements of the CRM component
21 in the MMF on the high cloud bias found in this study.

1 **Acknowledgments.** The authors thank Anthony T. Hoang for assistance with data
2 transfer and storage. The authors also express their appreciation to Jiundar Chern and
3 Wei-Kuo Tao for valuable discussions on the MMF and to Qiang Fu and Xianglei Huang
4 for comments on the ice absorption coefficient. This work was supported through the
5 Department of Energy's Atmospheric Radiation Measurement which is directed from the
6 Biological and Environmental Research program at the Office of Science. This work was
7 performed under the auspices of the U.S. Department of Energy by Lawrence Livermore
8 National Laboratory under Contract DE-AC52-07NA27344.

References

- 1 Arakawa, A. (1969), Parameterization of cumulus convection, in *Proc. WMO/IUGG*
2 *Symp. On Numerical Weather Prediction, IV, 8, 1–6*, Japen Meteorological Agency,
3 Tokyo, Japen.
- 4 Arakawa, A. (1975), Modeling clouds and cloud processes for use in climate model., in
5 *The Physical Basis of Climate and Climate Modeling*, vol. 16, pp. 183–94, GARP Pub-
6 lications Series, ICSU/WMO.
- 7 Arakawa, A. (2004), The cumulus parameterization problems: past, present, and future,
8 *J. Climate*, *17*, 2493–2525.
- 9 Chang, A. T. C., L. S. Chiu, and G. Yang (1995), Diurnal cycle of oceanic precipitation
10 from SSM/I data, *Mon. Wea. Rev.*, *123*, 3371–3380.
- 11 Chen, S. S., and R. A. J. Houze (1997), Diurnal variation and lifecycle of deep convective
12 systems over the Pacific warm pool, *Quart. J. Roy. Meteor. Soc.*, *123*, 357–388.
- 13 Collins, W. D., P. J. Rasch, B. A. Boville, J. J. Hack, J. R. McCaa, D. L. Williamson, B. P.
14 Briegleb, C. M. Bitz, S.-J. Lin, and M. Zhang (2006), The formulation and atmospheric
15 simulation of the community atmosphere model version 3 (CAM3), *J. Atmos. Sci.*, *19*,
16 2144–2161.
- 17 Dai, A. (2001), Global precipitation and thunderstorm frequencies. part II: Diurnal vari-
18 ations, *J. Climate*, *14*, 1112–1128.
- 19 Dai, A., F. Giorgi, and K. Trenberth (1999), Observed and model-simulated diurnal cycles
20 of precipitation over the contiguous United States, *J. Geophys. Res.*, *104*, 6377–6402.
- 21 Del Genio, A. D., M.-S. Yao, and J. Jonas (2007), Will moist convection be stronger in a
22 warmer climate?, *Geophys. Res. Lett.*, *34*, L16703, doi:10.1029/2007GL030525.

- 1 DeMott, C. A., D. A. Randall, and M. Khairoutdinov (2007), Convective precipitation
2 variability as a tool for general circulation model analysis, *J. Climate*, *20*, 91–112.
- 3 Ebert, E. E., and J. A. Curry (1992), A parameterization of ice cloud optical properties
4 for climate models, *J. Geophys. Res.*, *97(D4)*, 3831–3836, 10.1029/91JD02472.
- 5 Grabowski, W. (2001), Coupling cloud processes with the large-scale dynamics using the
6 cloud-resolving convection parameterization (CRCP), *J. Atmos. Sci.*, *58*, 978–997.
- 7 Grabowski, W., and P. Smolarkiewicz (1999), A cloud resolving convection parameteriza-
8 tion for modeling the tropical convective atmosphere, *Physica D*, *133*, 171–178.
- 9 Gray, W., and R. Jacobson (1977), Diurnal variation of deep cumulus convection, *Mon.*
10 *Wea. Rev.*, *105*, 1171–1188.
- 11 Hall, T. J., and T. H. V. Haar (1999), The diurnal cycle of west Pacific deep convection
12 and its relation to the spatial and temporal variations of tropical MCSs, *J. Atmos. Sci.*,
13 *56*, 3401–3415.
- 14 Haynes, J., R. Marchand, Z. Lou, A. Bodas-Salcedo, and G.L.Stephens (2007), A multi-
15 purpose radar simulation package: Quickbeam, *Bull. Amer. Meteorol. Soc.*, *88*, 1723–
16 1727.
- 17 Hendon, H. H., and K. Woodberry (1993), The diurnal cycle of tropical convection, *J.*
18 *Geophys. Res.*, *98*, 16,623–16,537.
- 19 Hong, G., G. heygster, and C. A. M. Rodriguez (2006), Effect of cirrus clouds on
20 the diurnal cycle of tropical deep convective clouds, *J. Geophys. Res.*, *111*, D06209,
21 DOI:10.1029/2005JD006208.
- 22 Houghton, J., Y. Ding, D. Griggs, M. Noguera, P. van der Linden, X. Dai, K. Maskell, and
23 C. Johnson (2001), *Climate Change 2001: The Scientific Basis*, Cambridge University

- 1 Press, 881pp.
- 2 Khairoutdinov, M. F., and D. A. Randall (2001), A cloud resolving model as a cloud
3 parameterization in the NCAR Community Climate Model: Preliminary results, *Geo-*
4 *phy. Res. Let.*, *28*, 3617–3620.
- 5 Khairoutdinov, M. F., and D. A. Randall (2003), Cloud resolving modeling of the ARM
6 summer 1997 IOP: model formulation, results, uncertainties and sensitivities, *J. Atmos.*
7 *Sci.*, *30*, 607–625.
- 8 Khairoutdinov, M. F., D. A. Randall, and C. DeMott (2005), Simulations of the atmo-
9 spheric general circulation using a cloud-resolving model as a superparameterization of
10 physical processes, *J. Atmos. Sci.*, *62*, 2136–2154.
- 11 Klein, S. A., and C. Jakob (1999), Validation and sensitivities of frontal clouds simulated
12 by the ECMWF model, *Mon. Wea. Rev.*, *127*, 2514–2531.
- 13 Kraus, E. B. (1963), The diurnal precipitation change over the sea, *J. Atmos. Sci.*, *20*,
14 551–556.
- 15 Kummerow, C., W. Barnes, T. Kozu, J. Shiue, and J. Simpson (1998), The tropical
16 rainfall measuring mission (TRMM), *J. Atmos. Oceanic Technol.*, *15*, 809–817.
- 17 Liu, C., and E. J. Zipser (2008), Diurnal cycles of precipitation, clouds and lightning in
18 the tropics from 9 years of TRMM observations, *Geophys. Res. Let.*
- 19 Liu, C., E. J. Zipser, and S. W. Nesbitt (2007), Global distribution of tropical deep
20 convection: different perspectives from TRMM infrared and radar data, *J. Climate*, *20*,
21 489–503.
- 22 Liu, G., J. A. Curry, and R.-S. Sheu (1995), Classification of clouds over the western equa-
23 torial Pacific ocean using combined infrared and microwave satellite data, *J. Geophys.*

- 1 *Res.*, *100*, 13,811–13,826.
- 2 Marchand, R., J. Haynes, G. G. Mace, T. Ackerman, and G. Stephens (2007), A compar-
3 ison of CloudSat cloud radar observations with simulated cloud radar output from the
4 Multiscale Modeling Framework global climate model, in preparation.
- 5 Marshall, J. S., and W. M. Palmer (1948), The distribution of rain drops with size, *J.*
6 *Meteor.*, *5*, 165–166.
- 7 McFarlane, S. A., J. H. Mather, and T. P. Ackerman (2007), Analysis of tropical radiative
8 heating profiles: A comparison of models and observations, *J. Geophys. Res.*, *112*,
9 D14218, DOI:10.1029/2006JD008290.
- 10 Mitchell, D. L., S. K. Chai, Y. Liu, A. J. Heymsfield, and Y. Dong (1996), Modeling cirrus
11 clouds. part I: Treatment of bimodal size spectra and case study analysis, *J. Atmos.*
12 *Sci.*, *53*, 2952–2966.
- 13 Miura, H., M. Satoh, H. Tomita, T. Nasuno, S. Iga, and A. T. Noda (2007), A short-
14 duration global cloud-resolving simulation with a realistic land and sea distribution,
15 *Geophys. Res. Let.*, *34*, L02804, doi:10.1029/2006GL027448.
- 16 Morcrette, J.-J. (1991), Evaluation of model-generated cloudiness: Satellite-observed and
17 model-generated diurnal variability of brightness temperature, *Mon. Wea. Rev.*, *119*,
18 1205–1224.
- 19 Nesbitt, S., and E. J. Zipser (2003), The diurnal cycle of rainfall and convective intensity
20 according to three years of TRMM measurements, *J. Climate*, *16*, 1456–1475.
- 21 Nesbitt, S., E. J. Zipser, and D. J. Cecil (2000), A census of precipitation features in the
22 tropics using TRMM: Radar, ice scattering, and lightning observations, *J. Climate*, *13*,
23 4087–4106.

- 1 Ovtchinnikov, M., T. Ackerman, R. Marchand, and M. Khairoutdinov (2006), Evalua-
2 tion of the Multiscale Modeling Framework using data from the atmospheric radiation
3 measurement program, *J. Climate*, *19*, 1716–1729.
- 4 Pauluis, O., and S. Garner (2006), Sensitivity of radiative-convective equilibrium simula-
5 tions to horizontal resolution, *J. Atmos. Sci.*, *63*, 1910–1923.
- 6 Randall, D. A., Harshvardhan, and D. A. Dazlich (1991), Diurnal variability of the hy-
7 drologic cycle in a general circulation model, *J. Atmos. Sci.*, *48*, 40–62.
- 8 Randall, D. A., M. F. Khairoutdinov, A. Arakawa, and W. W. Grabowski (2003), Breaking
9 the cloud-parameterization deadlock, *Bull. Amer. Meteorol. Soc.*, *84*, 1547–1564.
- 10 Richards, F., and P. A. Arkin (1981), On the relationship between satellite observed cloud
11 cover and precipitation, *Mon. Wea. Rev.*, *109*, 1081–1093.
- 12 Rosenfeld, D., and I. M. Lensky (1998), Satellite-based insights into precipitation forma-
13 tion processes in continental and maritime convective clouds, *Bull. Amer. Meteor. Soc.*,
14 *79*, 2457–2476.
- 15 Short, D. A., and J. M. Wallace (1980), Satellite-inferred morning-to-evening cloudiness
16 changes, *Mon. Wea. Rev.*, *108*, 1160–1169.
- 17 Short, D. A., P. A. Kucera, B. S. Ferrier, J. C. Gerlach, S. A. Rutledge, and O. W. Thiele
18 (1997), Shipboard radar rainfall patterns within the TOGA COARE IFA, *Bull. Amer.*
19 *Meteorol. Soc.*, *115*, 2817–2836.
- 20 Slingo, A. (2004), Simulation of the diurnal cycle in a climate model and its evaluation
21 using data from Meteosat 7, *Quart. J. Roy. Meteor. Soc.*, *130*, 1449–1467.
- 22 Soden, B. J., and F. P. Bretherton (1993), Upper tropospheric relative humidity from the
23 GOES 6.7 μm channel: Method and climatology for July 1987, *J. Geophys. Res.*, *98*,

- 1 16,669–16,688.
- 2 Soden, B. J., and F. P. Bretherton (1996), Interpretation of TOVS water vapor radiance
3 in terms of layer average relative humidities: Method and climatology for the upper,
4 middle and lower troposphere, *J. Geophys. Res.*, *101*, 9333–9343.
- 5 Soden, B. J., S. Tjemkes, J. Schmetz, R. Saunders, J. Bates, B. Ellingson, R. Enge-
6 len, L. Garand, D. Jackson, G. Jedlovec, T. Kleespies, D. Randel, P. Rayer, E. Salathe,
7 D. Schwarzkopf, N. Scott, B. Sohn, S. de Souza-Machado, L. Strow, D. Tobin, D. Turner,
8 P. van Delst, and T. Wehr (2000), An intercomparison of radiation codes for retriev-
9 ing upper-tropospheric humidity in the 6.3- μ m band: A report from the first GVaP
10 workshop, *Bull. Amer. Meteorol. Soc.*, *81*, 797–808.
- 11 Sui, C.-H., K.-M. Lau, Y. N. Takayabu, and D. A. Short (1997), Diurnal variation in
12 tropical oceanic cumulus convection during TOGA COARE, *J. Atmos. Sci.*, *54*, 639–
13 655.
- 14 Tao, W.-K., J. Chern, R. Atlas, D. Randall, X. Lin, M. Khairoutdinov, J.-L. Li, D. E.
15 Waliser, A. Hou, C. Peters-Lidard, W. Lau, and J. Simpson (2007), A multi-scale
16 modeling system: Developments, applications and critical issues, *J. Geophys. Res.*,
17 submitted.
- 18 Tian, B., B. J. Soden, and X. Wu (2004), Diurnal cycle of convection, clouds, and water
19 vapor in the tropical upper troposphere: Satellites versus a general circulation model,
20 *J. Geophys. Res.*, *109*, D10101, DOI:10.1029/2003JD004117.
- 21 Wyant, M. C., M. Khairoutdinov, and C. S. Bretherton (2006), Climate sensitivity
22 and cloud response of a GCM with a superparameterization, *Geophys. Res. Lett.*, *33*,
23 L06714, DOI:10.1029/2005GL025464.

- 1 Yang, G.-Y., and J. M. Slingo (2001), The diurnal cycle in the tropics, *Mon. Wea. Rev.*,
- 2 *129*, 784–801.
- 3 Zipser, E. J., D. J. Cecil, C. Liu, S. W. Nesbitt, and D. P. Yorty (2006), Where are the
- 4 most intense thunderstorms on earth?, *Bull. Amer. Meteorol. Soc.*, *87*, 1057–1071.

	$T_{11} > 260 \text{ K}$	$230 \text{ K} < T_{11} < 260 \text{ K}$	$T_{11} < 230 \text{ K}$
PI	0	0	$a_p(230-T_{11})$
CLD	0	1	1
UTH	$(\cos\theta/p_0)\exp(a+bT_{6.7})$	-999.	-999.

Table 1. Retrieval algorithm at each pixel (each CRM grid column) in each satellite (GCM) grid box of the resolution 2.5° longitude by 2.0° latitude. $a_p = 6.96 \text{ mm day}^{-1} \text{ K}^{-1}$. θ is the satellite zenith angle; p_0 term denotes the dependence of $T_{6.7}$ on air temperature; $a = 27.9$, and $b = -0.10$. “-999.” is missing value assumed for clear-sky UTH when cloudy.

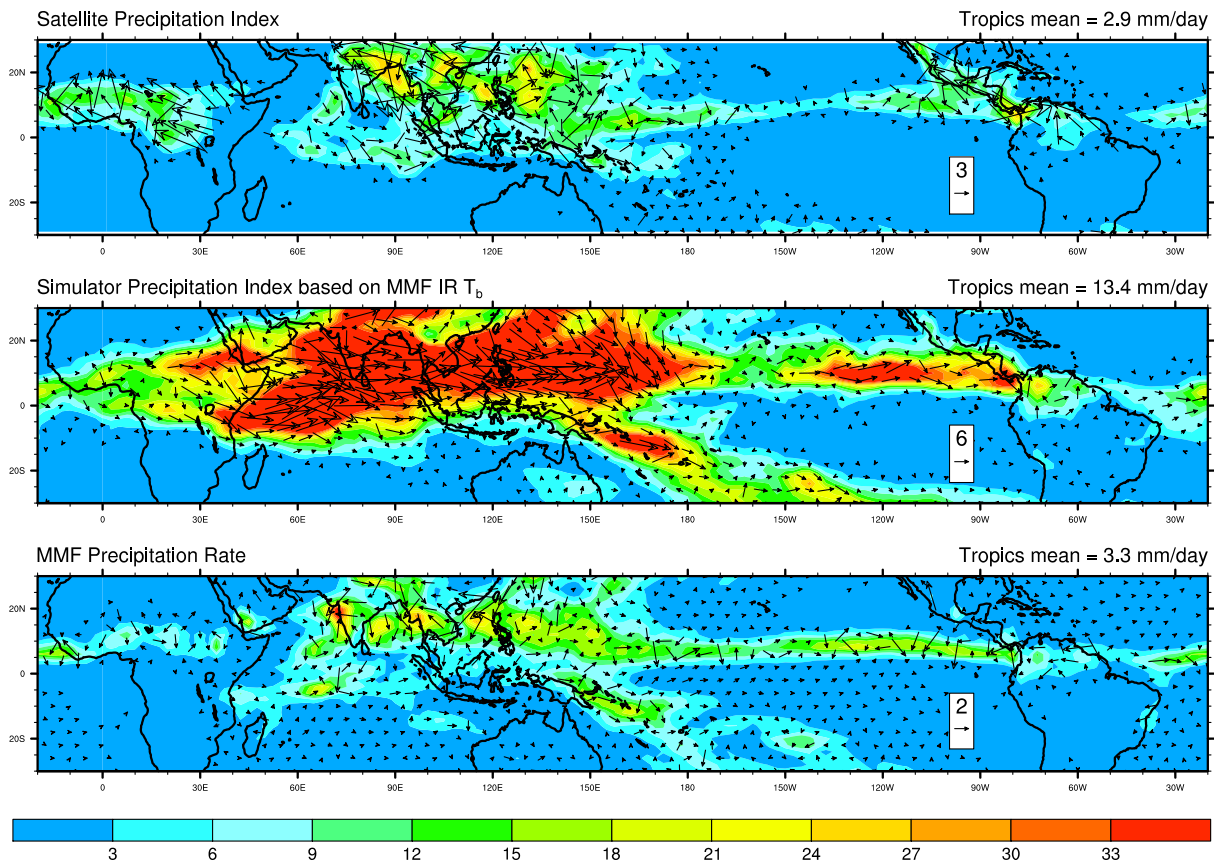


Figure 2. July 1999 daily means and the monthly mean diurnal cycles of precipitation index (PI) from geo-stationary satellite (top panel), PI from the IR T_b simulator applied to the MMF (middle panel), and the MMF actual surface precipitation rate (bottom panel). Color shading shows daily means in mm/day. Tropical (30°S to 30°N) mean values are shown at the up-right corner of each panel. The length of the vector denotes the diurnal amplitude (mm/day). Notice the different scales of the vector length in the legend of each panel. Diurnal phase is represented by a 24-hour clock: upward arrow for midnight (0000 LST), rightward for dawn (0600 LST), downward for noon (1200 LST) and leftward for dusk (1800 LST).

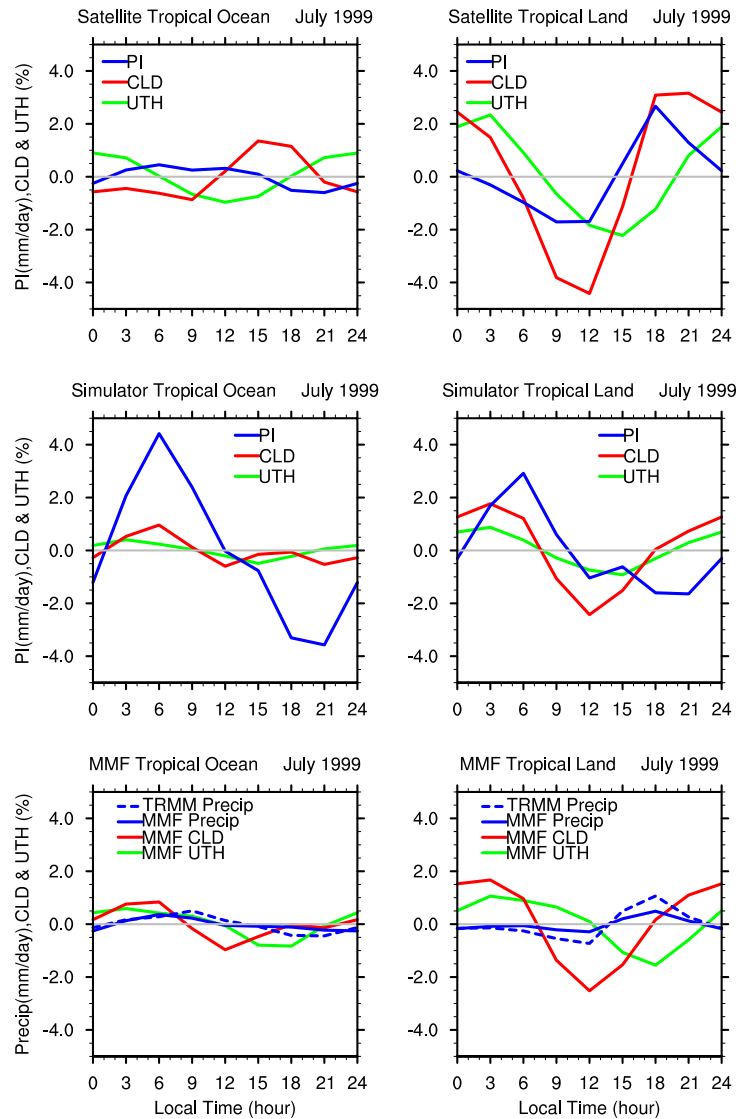


Figure 3. July 1999 diurnal anomalies of precipitation (solid blue), high clouds amount (CLD, in red) and upper tropospheric relative humidity (UTH, in green) for tropical land (right) and ocean (left). The top two panels show the precipitation index (PI), CLD and UTH based on geo-satellite observed T_b . The middle two panels show PI, CLD and UTH based on T_b from the infrared T_b simulator applied to the MMF. The bottom two panels show the MMF actual surface precipitation rate (solid blue), high cloud amount (solid red) and upper troposphere relative humidity (solid green) derived from the CRM cloud condensates and water vapor. The blue dashed lines in the bottom two panels are the surface precipitation rate retrieved from TRMM precipitation radar reflectivity.

	Satellite		MMF IR Simulator		MMF Actual		TRMM	PR
	Ocean	Land	Ocean	Land	Ocean	Land	Ocean	Land
PI (mm/day)	0.5	1.9	3.6	2.0	0.3	0.2	0.43	0.61
	[18%]	[55%]	[26%]	[17%]	[7.4%]	[9.8%]	[16%]	[24%]
	2.7	3.4	14.0	11.4	3.6	2.5	2.7	2.5
CLD (percent)	1	4	0.5	1.9	0.7	2.0		
	[9%]	[28%]	[2.5%]	[9%]	[2.7%]	[8.4%]		
	11	14	21.1	20.8	24.4	24.4		
UTH (percent)	1	2.2	0.4	0.8	0.7	1.2		
	[3%]	[6%]	[1%]	[2.3%]	[1.9%]	[3.2%]		
	33.3	36.7	35.9	36.2	36.1	38.5		

Table 2. July 1999 diurnal cycle statistics: bold text (first row in each cell) shows diurnal amplitude spatially-weighted averaged over tropical ocean and land respectively; percentage in brackets is the normalized diurnal amplitude by dividing the diurnal amplitude by the daily mean value; plain text (last row in each cell) is for daily means.

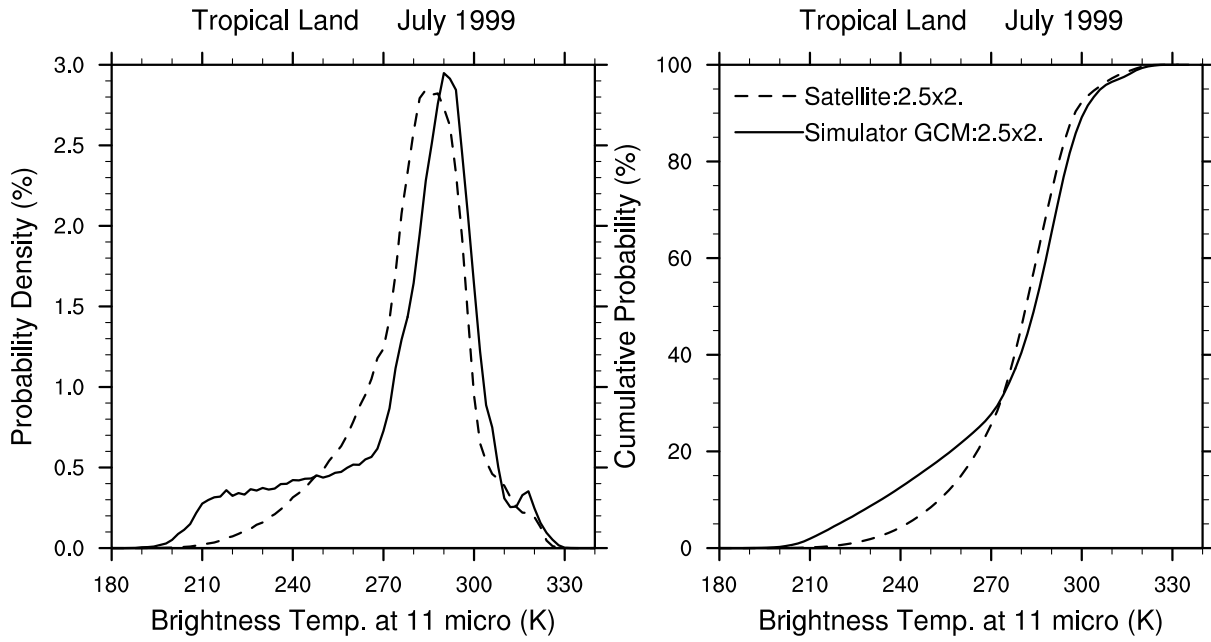


Figure 4. The probability density function (left) and cumulative probability (right) for the brightness temperatures at 11 micrometer, T_{11} , over land regions between 30°S and 30°N in July 1999. Dashed (solid) line is from geo-stationary satellite data (the IR T_b simulator applied to the MMF) at resolution of 2.5° longitude by 2° latitude.

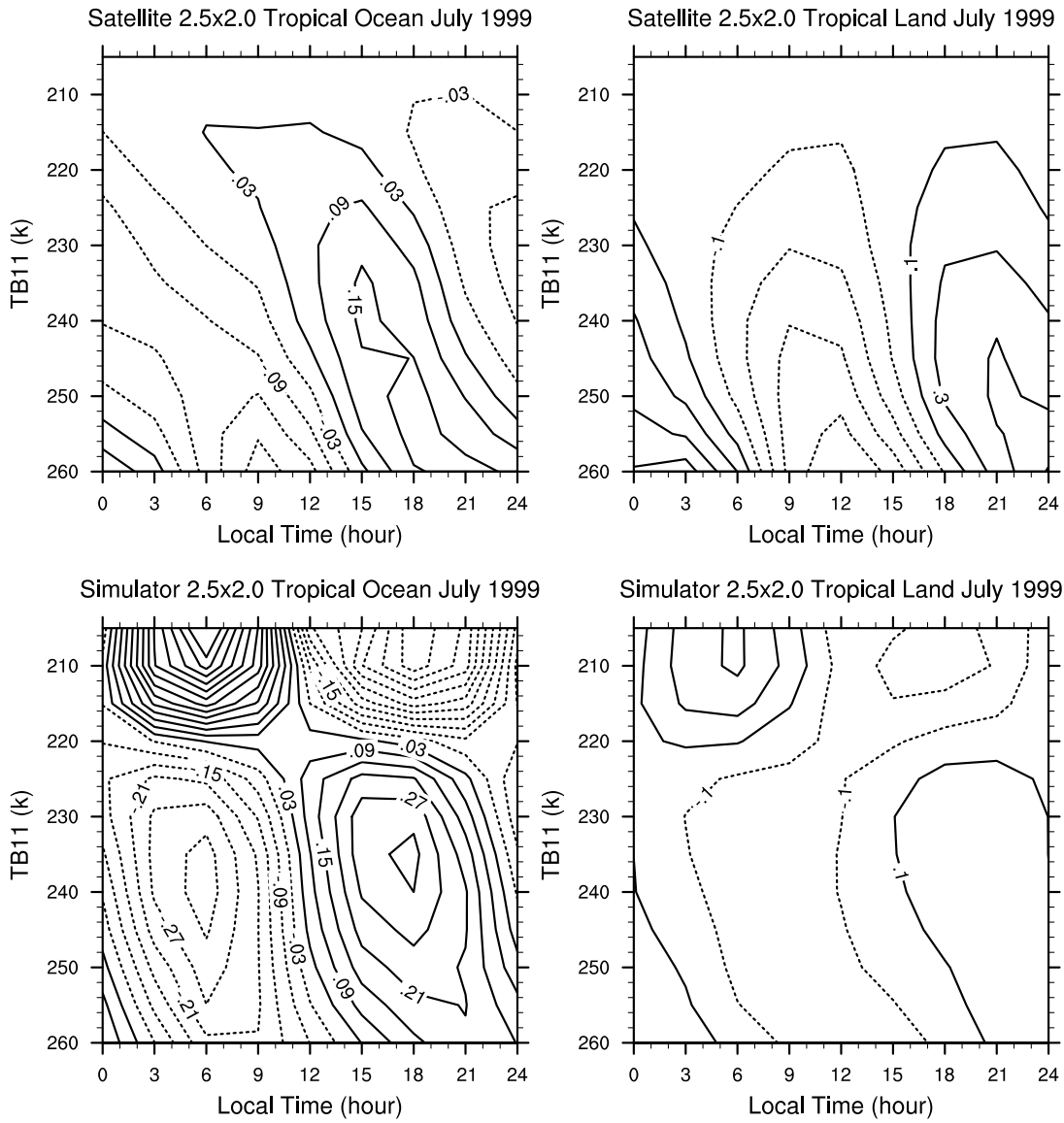


Figure 5. Histogram of the probability anomalies (in percent) for T_{11} to occur in each 5 k bin at certain local standard time in July 1999. Top (bottom) panels are from geo-stationary satellite data (the infrared T_b simulator applied to the MMF) at resolution of 2.5° longitude by 2° latitude. Left (right) columns are for tropical ocean (land). Notice that the contour line interval is 0.2 (0.06) percent over land (ocean) with negative values in dashed lines.

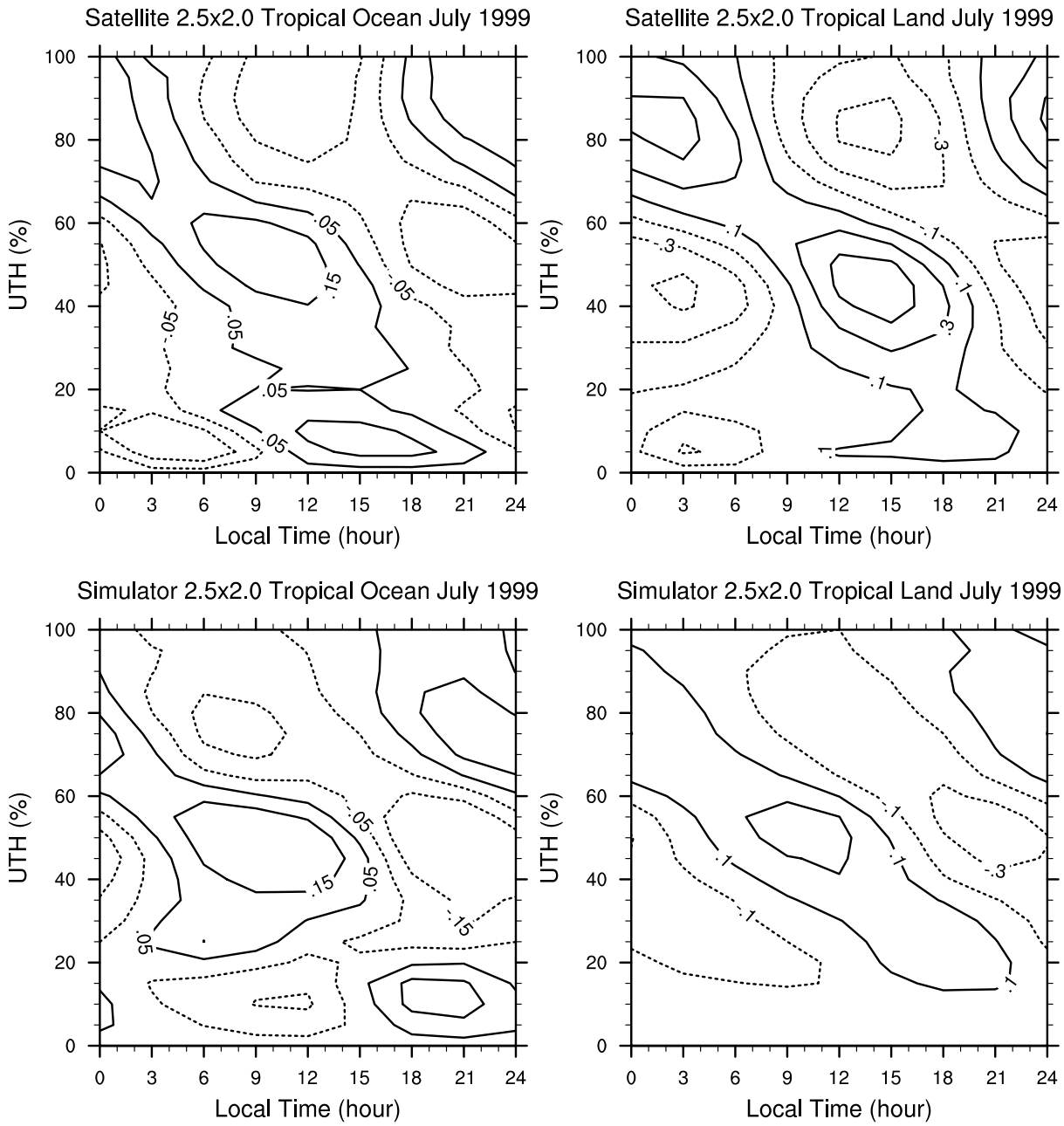


Figure 6. Same as in Figure 5, but for upper troposphere relative humidity (UTH) in its 5% bins.

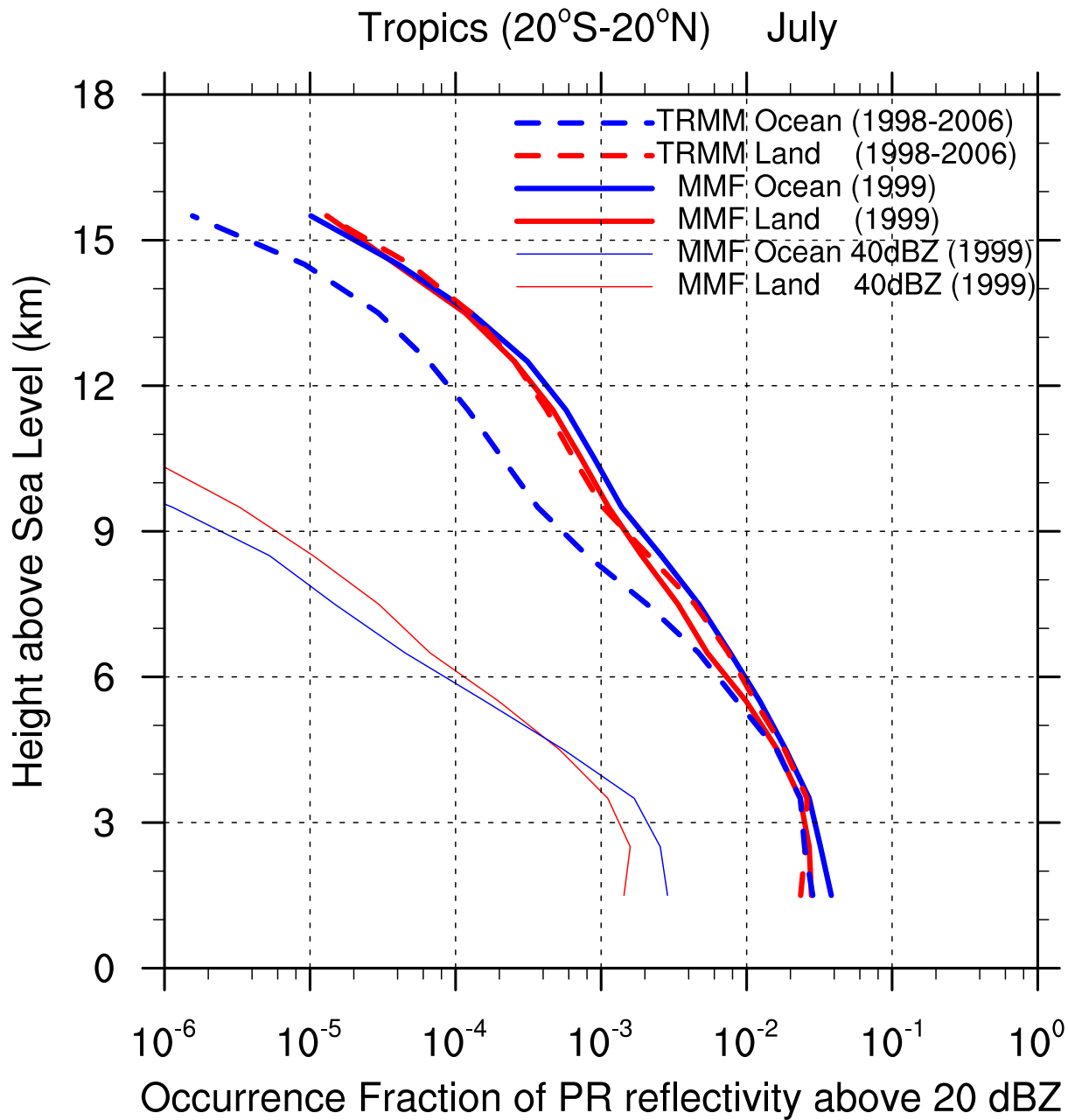


Figure 7. The occurrence fraction of precipitation radar (PR) reflectivity ≥ 20 dBZ in July in tropics (20°S-20°N). Blue (red) lines are for tropical ocean (land). Solid lines are from the PR simulator applied to the MMF CRM data in July 1999. Dashed lines are from the TRMM PR data in July averaged over the years 1998 to 2006. The MMF July 1999 40 dBZ or greater occurrence fractions are shown in thin lines. Note that the X-axis is in logarithmic scale.

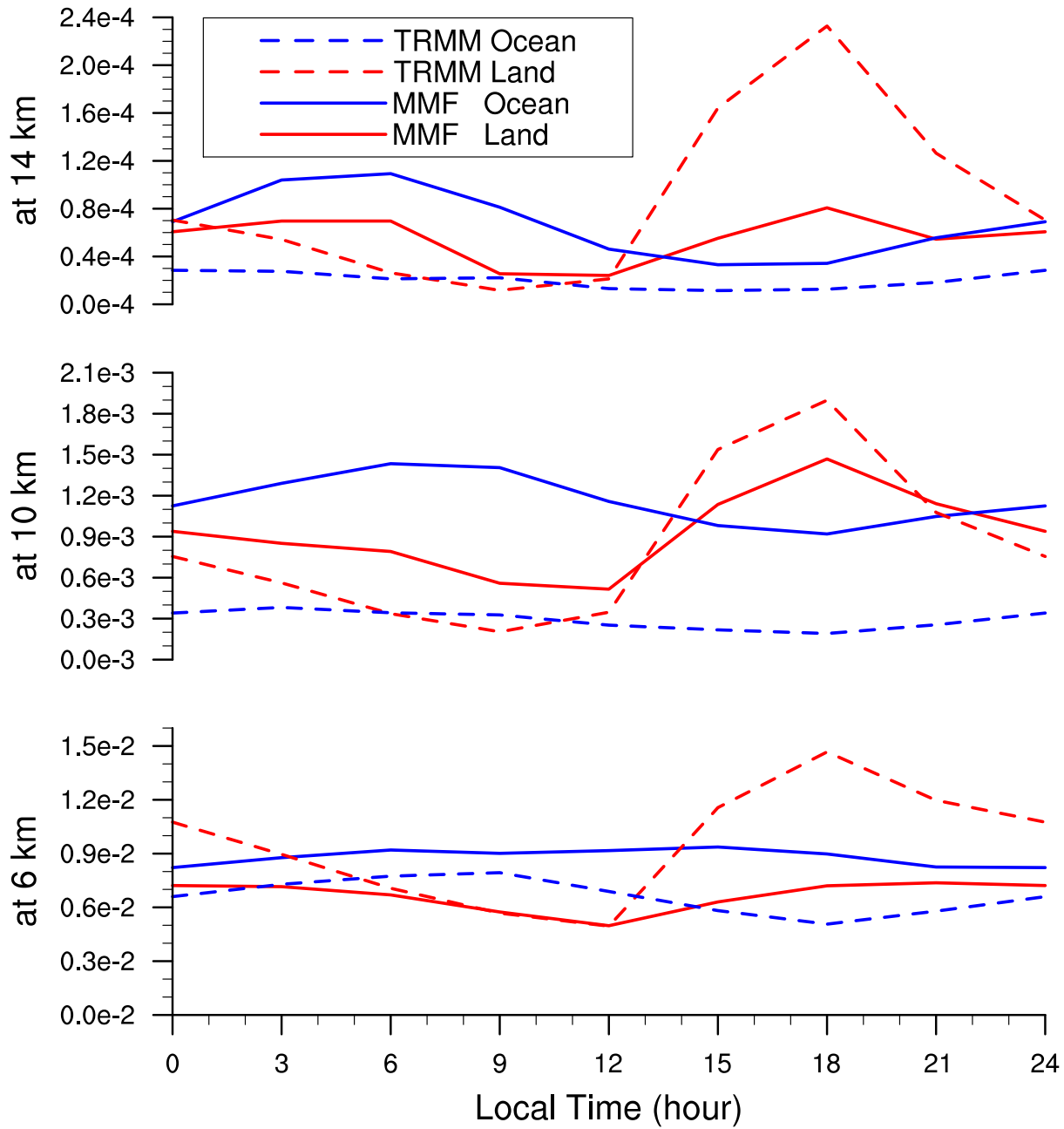


Figure 8. Diurnal cycle of the 20 dBZ or greater precipitation radar (PR) reflectivity occurrence fraction in July in 20°S-20°N at three height levels: 14 km (top), 10 km (middle) and 6 km (bottom). Blue (red) lines are for tropical ocean (land). Solid lines are from the PR simulator applied to the MMF CRM data in July, 1999. Dashed lines are from the TRMM PR data in July averaged in years 1998 to 2006.

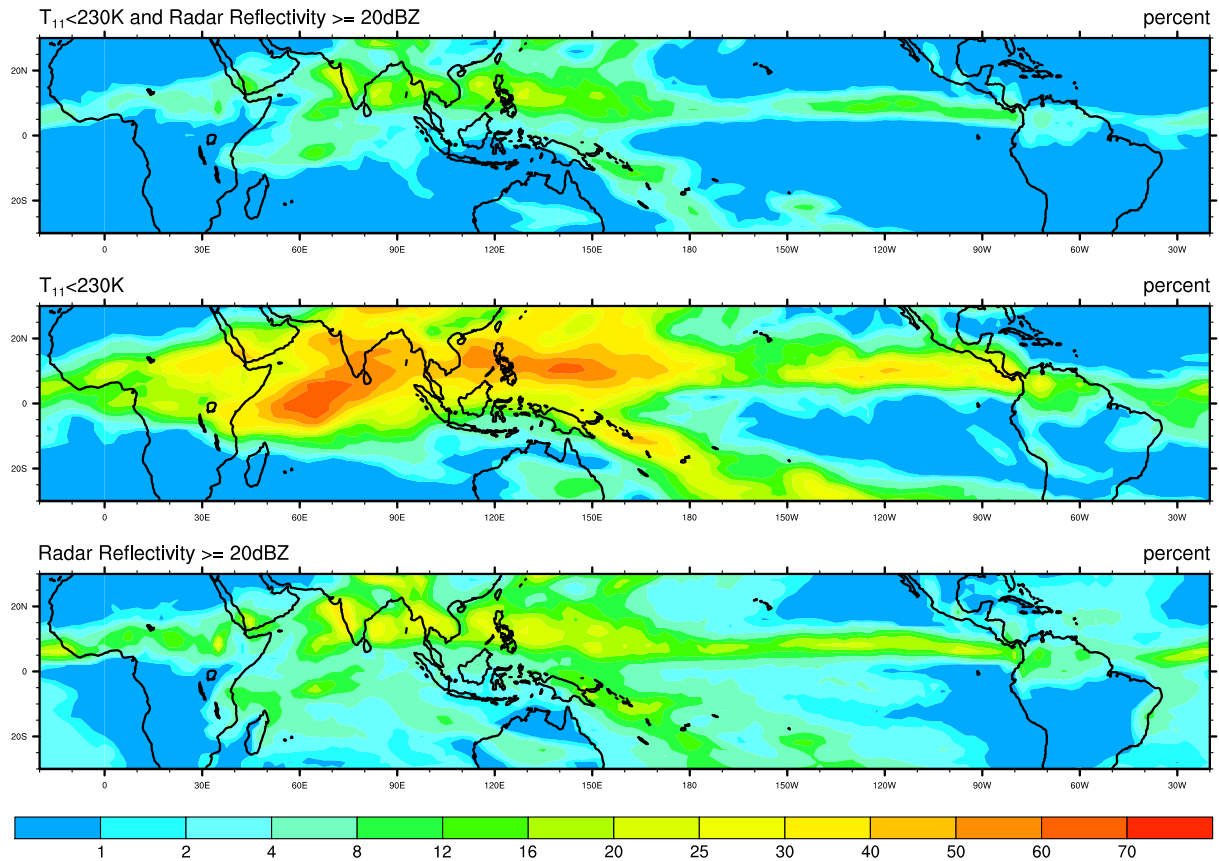


Figure 9. July 1999 daily mean probability (in percent) for simulators to detect CRM columns at each GCM grid box in the MMF: with IR $T_{11} < 230$ K and PR reflectivity ≥ 20 dBZ (top); with IR $T_{11} < 230$ K only (middle); with PR reflectivity ≥ 20 dBZ only (bottom).

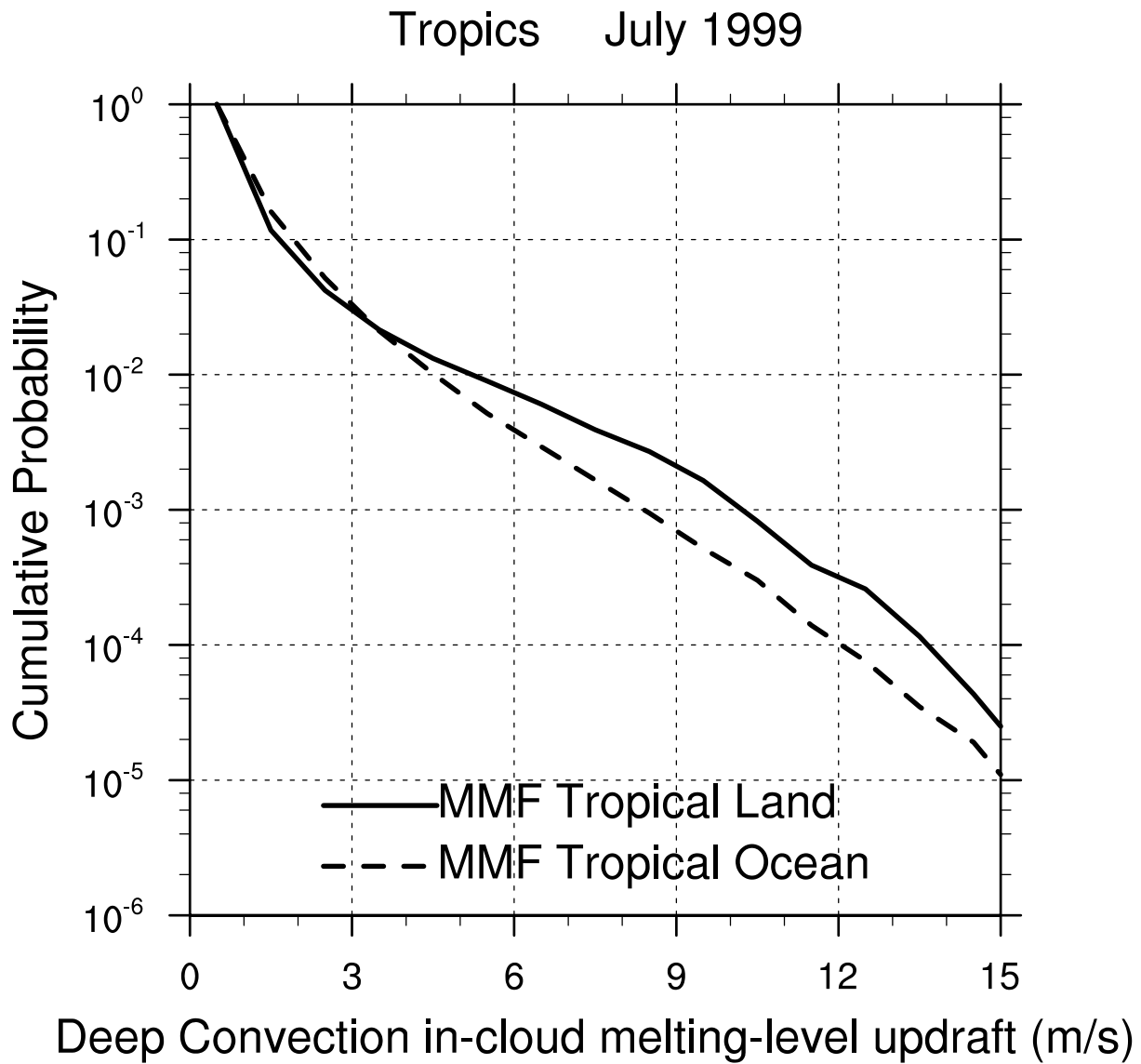


Figure 10. The cumulative probability of deep-convection in-cloud melting-level updraft, dashed line for ocean and solid line for land.

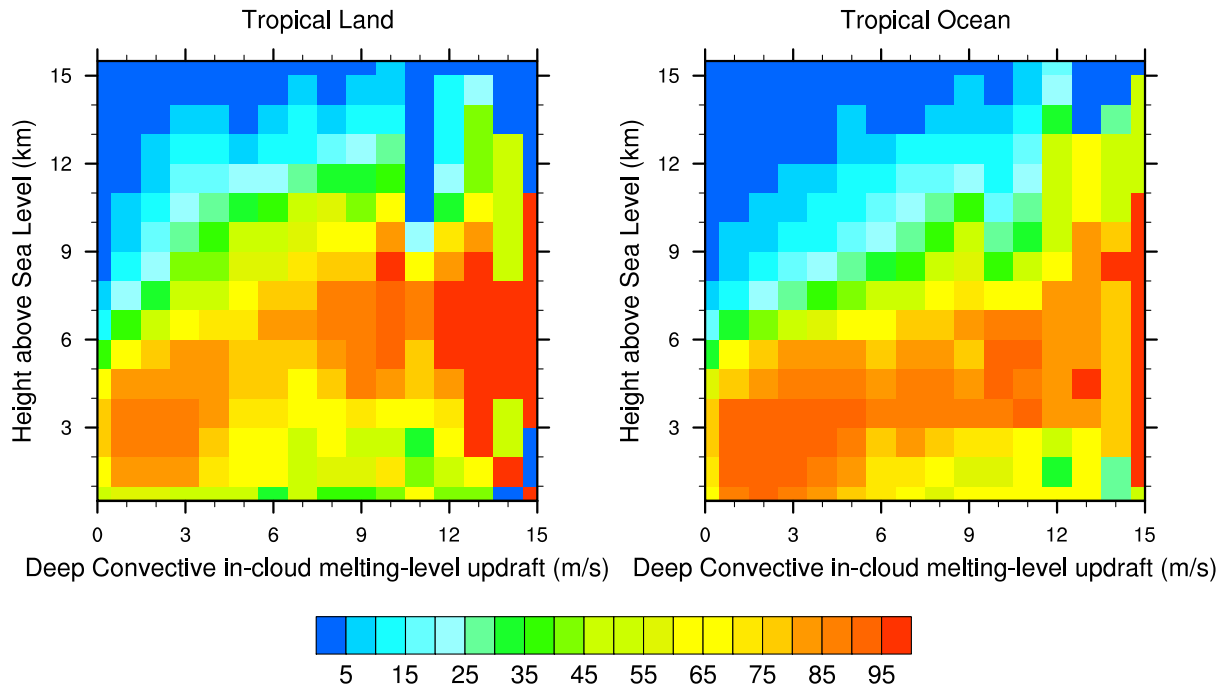


Figure 11. The probability (in percent) for PR reflectivity of 20 dBZ or greater to occur at a given height in each 1 m/s bin of deep-convective in-cloud melting-level updrafts.